ADVANCED FUNCTIONAL MATERIALS
www.afm-journal.de

Materials Views
www.MaterialsViews.com

Hierarchically Ordered Nano-Heterostructured PZT Thin Films with Enhanced Ferroelectric Properties

Anuja Datta, Devajyoti Mukherjee, Sarath Witanachchi, and Pritish Mukherjee*

Realization of ferroelectric (FE) devices based on the polarization effects of $Pb(Zr_{0.52}Ti_{0.48})O_3$ (PZT) has reinforced the investigation of this material in multiple dimensions and length scales. Multi-level hierarchical nanostructure engineering in PZT thin films offer dual advantages of variable length-scale and dimensionality. Here, the growth of hierarchically ordered PZT nano-heterostructures (Nhs) from PZT seed-layer deposited on $SrTiO_3$:Nb (100) substrates, using a physical/chemical combined methodology involving pulsed laser deposition (PLD) and hydrothermal processes, is reported. Systematic SEM, TEM, and Raman spectroscopy studies reveal mixed hetero- and homo-epitaxial growth mechanism. In the final stage, 3D Nh units cross-link and form a dense network-like Nh PZT thin-film. FE polarizations are measured without using any polymer fill-layer which otherwise introduces huge dielectric losses and lowers the polarization values for a FE device. In benefit, well saturated and symmetric FE hysteresis loops are observed with high degree of squareness and a high remnant polarization (54 μC cm^{-2} at a coercive field of 237 kV cm^{-1}). This work provides a pathway towards preparing hierarchical PZT Nhs offering coherent design of high-performance FE capacitors for data storage technologies in future.

1. Introduction

Since the discovery of ferroelectricity, various perovskite oxide materials have been widely investigated due to their spontaneous charge polarization and piezoelectricity.[1–3] Typically ferroelectric (FE) perovskite oxide materials exhibit long range alignment of electric dipoles resulting in a net polarization under an applied electric field.[2,3] Due to this property and other characteristics such as pyroelectricity and large dielectric constants, FE materials have potentially become essential components in a wide spectrum of applications such as nonvolatile random access memory (NVRAM) and micro-electro-mechanical (MEMs) devices.[3] They are also being explored for various sensor and actuator applications as high-frequency electrical components and tunable microwave circuits.[1–4]

Among the classical perovskite oxide materials, $Pb(Zr_{0.52}Ti_{0.48})O_3$ (PZT) has been extensively studied for its highest FE polarization and piezoelectric coefficient.[5–8] PZT is also a technologically important FE material due to its high mechanical and chemical stability.[8–10] Realization of devices based on FE properties of PZT has reinforced the investigation of this material in thin-film form.[3,5,6,8–13] However, research in FE thin films is limited due to intrinsic difficulties of structural engineering in thin films particularly in the nano-scale. To this end, nano-heterostructured (Nh) thin films of FE materials, in general, exhibit uniquely different properties from non-textured homogenous thin films due to the deliberate engineering of nano-scale features into the structure of the films.[14–19] Furthermore, it is commonly believed that high surface area achieved through multi-level 2D and 3D nanostructure engineering in thin films plays a salient role in achieving high structural and property efficiency compared to regular 1D nanostructured films.[20–22] Recent reports have emphasized the control of arrangements of nano-sized building blocks into hierarchical structures of pervoskite materials leading to oriented-attachment and self-assembly.[23–26] Efforts to synthesize and understand FE properties of PZT 1D nanostructured thin films have been boosted because of the promise they show in the realization of nano- and micro-scale devices.[14–16,27–32] It was observed that the properties of interest for PZT at the nano-scale range are governed by the crystal structure and orientation of the crystallized surface facets.[16,27–32] FE polarization was measured from PZT 1D nanotubes embedded in porous alumina membrane (PAM) suggesting pronounced dimensionality effect in this material in ordered nanostructured form.[17] Therefore, integration of FE PZT nanostructured thin films with ordered 2D and 3D periodic structures, controlled exposed facets, and crystal orientations of the nanostructures could be of immense significance, although particularly challenging to synthesize.

In the present work, we report on the directed growth of PZT hierarchical nano-heterostructures (HNh) promoted by PZT seed-assisted nucleation and controlled orientation. An innovative physical/chemical combined synthetic-strategy involving pulsed laser deposition (PLD) technique and hydrothermal

---

Dr. A. Datta, Dr. D. Mukherjee, Prof. S. Witanachchi,
Prof. P. Mukherjee
Florida Cluster for Advanced Smart Sensor
Technologies & Department of Physics
University of South Florida
Tampa, FL 33620, USA
E-mail: datta@usf.edu

Dr. D. Mukherjee, Prof. S. Witanachchi, Prof. P. Mukherjee
Center for Integrated Functional Materials & Department of Physics
University of South Florida
Tampa, FL 33620, USA

DOI: 10.1002/adfm.201303290

© 2014 WILEY-VCH Verlag GmbH & Co. KGaA, Weinheim

process was explored for the first time in order to obtain structure and orientation-selective synthesis of oriented PZT HNhs over large area substrates. As an advanced tool for growing high quality complex oxide thin films, PLD has made a significant impact in terms of growth of single- and multi-layered heterostructures of multi-component materials.[6–8,10,13] In our approach, PLD guaranteed uniform deposition of PZT seed-layer thin films while chemical after-treatment of the seed-layer ensured controlled growth of the nanostructures thereby bringing out the advantages of both the processes.[18] The key aspect of this unique growth process results in hierarchical 3D PZT nanostructured thin films in which the Nhs self-orient to form a highly compact and dense network-structure. This facilitates the measurement of the FE properties of these nanostructured thin films without using any organic fill-layer or template, which has so far been a common practice.[17] As a positive effect of the increased compliance of the HNhs, we observed well-saturated and symmetric FE hysteresis loops with high degree of squareness and enhanced remanent polarization, a major improvement over FE properties as reported from other PZT nanostructures.[17] Moreover, given the current absence of a facile method for preparing hierarchical PZT micro-/nanostructures, our approach reported here represents an important advancement with potential impact in many technological applications requiring the use of hierarchical structures of FE materials.

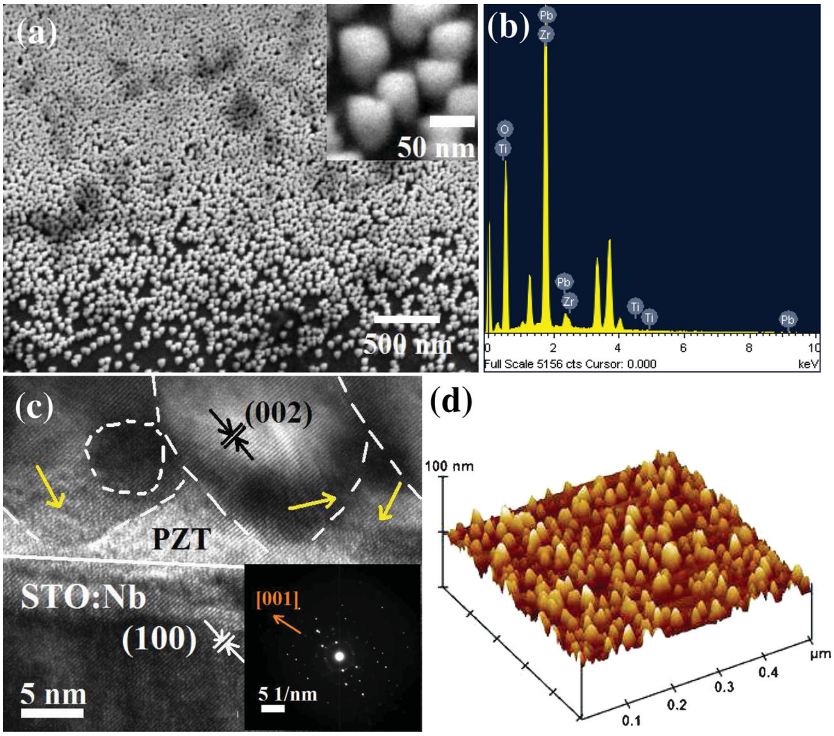

Figure 1. a) SEM image of the PZT seed-layer (50 nm thickness) deposited on STO:Nb substrate by pulsed laser deposition. The inset shows the tooth-like geometry of the PZT nano-seeds with a lateral dimension and height of 50 nm each. b) Representative EDS spectrum of the stoichiometric PZT seed-layer confirmed from different regions on the thin-film surface. c) Cross-sectional high resolution TEM image of the PZT seed-layer on STO:Nb substrate showing the growth of PZT tooth-like seeds with a preferred (00*l*) orientation that maintains a clean interface with the STO:Nb (100) substrate. Locally other growth planes in tetragonal PZT structure were noticed (shown by the dashed circle). Arrows indicate the misfit dislocation planes observed in places in PZT seed-layer near the film-substrate interface. d) AFM image of the surface of the PZT seed-layer that matches the average seed size as observed by SEM and TEM.

2. Results and Discussion

2.1. Structural Study of PZT Seed-Layer Deposited by PLD

The starting point for the growth of PZT hierarchical nanostructures is initiated by the deposition of compact PZT seed-layer on Nb-doped $SrTiO_3$ (STO:Nb) (100) substrates by the PLD process using optimized parameters.[12,13] The SEM images of the PZT seed-layer thin-film, from an area of least coverage on the film surface indicates tooth-like geometry of the PZT seeds (**Figure 1**a) with clearly-developed facets (inset to Figure 1a). The average size of the PZT seeds varies from <5 nm at the bottom to ≈50 nm at the top, with the typical thickness of the seed-layer film of ≈50 nm. Compositional analysis by EDS (Figure 1b) revealed stoichiometric distribution of the constituent atoms when recorded from individual PZT seed and from different areas of the thin-film surface (Figure 1b). Cross-sectional TEM image of the seed-layer film (Figure 1c) provides insight into the distribution, morphology and crystallinity of the PZT seeds on STO:Nb substrate. Closely-spaced tooth-like growth of PZT seeds were observed from the cross-sectional TEM image. The formation of a predominating growth of (00*l*) ($l = 0,1,2$) planes of PZT on the STO:Nb substrate was observed from the HRTEM image in Figure 1c. The close matching of lattice parameters of PZT (tetragonal, $a = 4.055$ Å, $c = 4.11$ Å) and STO:Nb (cubic, $a = 3.905$ Å) allows for such textured growth of PZT seed-layer.[12,13] The TEM analysis of the sample revealed a well-defined and atomically sharp interface of the PZT seed-layer with STO:Nb substrate. However, as can be observed from Figure 1c, some areas have misfit dislocations (shown by arrows in Figure 1c), which might form due to relaxation of the lattice mismatch strain between the PZT nanocrystalline seeds and the substrate during the PLD process.[35] Lattice planes from other orientations are also observed as marked (circle) in Figure 1c and selected area electron diffraction pattern (SAED) from the PZT seed-layer shows preferentially oriented lattice planes with signatures of polycrystallinity (inset to Figure 1c). Figure 1d shows an AFM image of the surface morphology of the PZT seed-layer captured at a region where the seeds are sparsely distributed. As is clearly evident from the figure the seed-layer is not continuous in this region. However, uniform grains of about 42 ± 13 nm in diameter and about 40 ± 5 nm in height are distributed over the surface. The

© 2014 WILEY-VCH Verlag GmbH & Co. KGaA, Weinheim

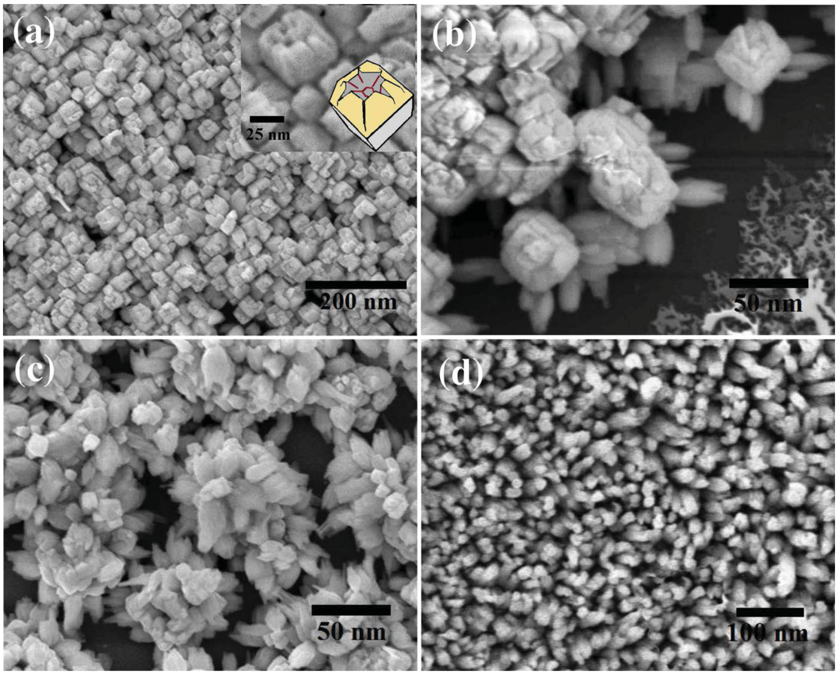

Figure 2. SEM images of the hierarchical PZT nano-heterostructure growth after the hydrothermal treatment of PZT nano-seeds at different time-periods. a) Nano-stub-like growth with emerging branches of PZT with a 10 nm tip-diameter (inset) from the top-surface of the PZT nano-seeds after 2h. Inset shows a dimensional scheme of the nano-stub structure. b) First-order hierarchical growth from PZT nano-stubs showing the growth of branches of 10 nm in size (tip diameter) after 4 h. c) Further hierarchical growth and formation of flower-like morphology after 6 h. d) Dense growth of PZT nano-branches after 8 h of hydrothermal treatment.

root-mean-square roughness (R_{rms}) value for the seed-layer was 8 ± 2 nm. It is noted that the tips of the seeds here appear to be rounded and pointed (as opposed to flat tips in the SEM image in Figure 1a). This is due to the fact that the AFM tip was used in the "non-contact tapping mode" during the scans in order to avoid the crashing of the tip against the surface features of the PZT seed-layer.

2.2. Time-Dependent Structural Evolution of PZT HNh

After the hydrothermal treatment of the seed-layer thin-film, PZT Nhs started to grow from the PZT seeds, which were optimized after several synthesis stages as determined by reaction times. Samples at 2 h reaction-time intervals were collected and characterized by SEM and Raman. Initially, the sample obtained after 2 h of hydrothermal reaction showed the dense formation of PZT stubs with a tetragonal base (**Figure 2**a and the inset). The stub-like growth was uniform and had homogenous surface coverage with negligible variations in the morphology. The average size of these stub-like structures (scheme in the inset of Figure 2a) was ≈50 nm (diagonal dimension of the square base of the stub), commensurate with the top dimension of the PZT seeds (inset to Figure 2a). The initiation of the hierarchy from these structures was observed in the sample obtained after 4 h (Figure 2b). Nanorod branches grew out of the nano-stub bases to form first-order hierarchical structures (Figure 2b) and after 6 h of reaction, these structures grew further into second order HNhs visually giving rise to a flower-like morphology (Figure 2c). Significantly, as the nano-stubs outgrew into primary and secondary nanorod branches from the tetragonal base, a network of PZT Nhs gradually covered the substrate surface. As shown in Figure 2d, these Nh networks were extremely dense locally and only the hierarchical branches were visible without exposing the bases after 8 h of hydrothermal reaction.

On increasing the hydrothermal reaction time to 10 h, further development in the hierarchy order was noticed in the PZT Nhs as shown in the SEM images in **Figure 3**a,b. In order to indicate the detailed microstructure of the higher order HNhs we have shown the SEM images (Figure 3a,b) taken from the sparsely populated peripheral regions of the films. Most of the film surface was covered by densely populated structures as shown in Figure 2d. From Figure 3b it is clearly observed that the hierarchical nanorod branches are embraced and truncated by sharp faces with rectangular cross-sections (Figure 3b). The highest order branches were <5 nm in cross-sectional dimension. Orientations of the hierarchies gave rise to an overall tetragonal morphology in the individual Nh (Figure 3b) and conformed to the tetragonal crystal structure of PZT. Furthermore, these tetragonal PZT HNh units demonstrate oriented-attachment in some areas of the sample as shown in Figure 3c, where four units attach together to form a larger tetragonal shaped Nh network. Higher order of interlocking attachment of the PZT hierarchical branches (Figure 3d) made the network more stable and denser after 12 h of hydrothermal reaction. As shown in Figure 3e, the interlocking branches of the hierarchical PZT Nhs along with the increasing growth period increased the filling rate within the spaces of neighboring Nhs providing a densely packed nanostructured film surface with enhanced surface area (Figure 3e and see Supporting Information Figure S1).

The θ–2θ XRD pattern of the dense and compact PZT HNh film (Figure 3f) prepared after 12 h of hydrothermal treatment of the PZT seed-layer thin-film on STO:Nb indicated the formation of single-phase tetragonal PZT with *P4mm* (99) space group that co-exists with the STO ($l00$) ($l = 1,2,3$) peaks. The standard XRD patterns of tetragonal PZT (JCPDS Card # 01–070–4060) and of STO (JCPDS Card # 00–035–0734) are also shown in the figure for comparison. In contrast to the XRD pattern of the PZT seed-layer thin-film deposited by PLD (also included in Figure 3f) which invariably showed preferential c-axis orientation with dominating ($00l$) PZT peaks, the XRD pattern of the final PZT HNh thin-film mostly showed polycrystalline nature. This could be attributed to the different spatial orientation of the branches in the sample.

To elucidate the growth mechanism of these hierarchical PZT Nhs on STO:Nb substrates and to understand their density distribution on the substrate, systematic TEM study was

© 2014 WILEY-VCH Verlag GmbH & Co. KGaA, Weinheim

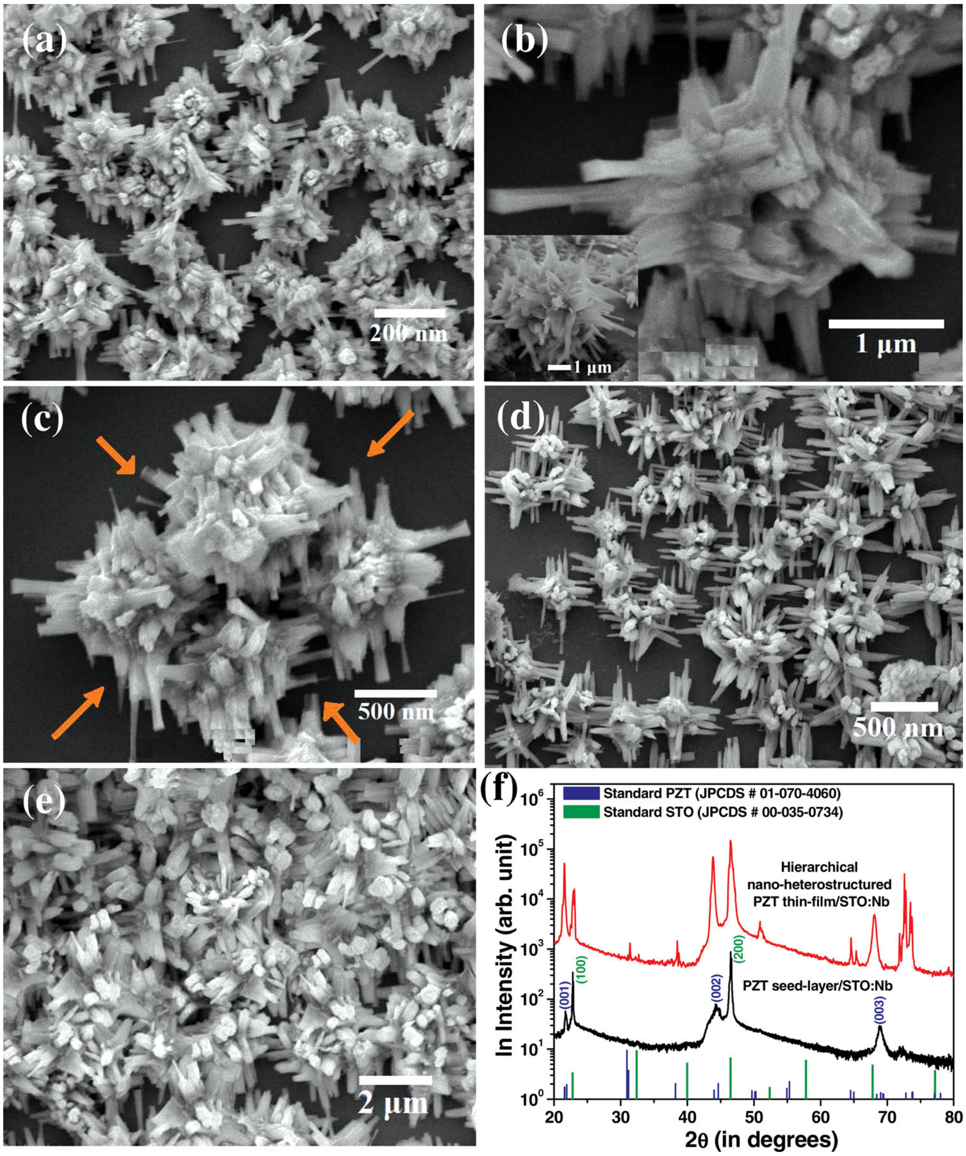

Figure 3. SEM images of the hierarchical growth of PZT nano-heterostructures (Nhs) after a,b,c) 10h and d,e) 12 h of hydrothermal treatment, respectively. The highest order hierarchical branch shown in (a,b) is < 5 nm (the tip size). The rectangular cross-section of the hierarchical branches confirm the crystal structure of PZT. The Nh units grow maintaining symmetrical tetragonal geometries. Inset to b) shows the 3D nature of the Nh unit. The tetragonally shaped Nh units form larger hierarchical tetragonal ensemble through oriented-attachment process. Cross-linking of the larger PZT tetragonal Nh ensembles forming a larger network increases the density of the thin-film creating a nearly non-porous surface after 12 h. f) XRD spectra of the PZT seed-layer showing a preferred (00*l*) growth and polycrystalline HNh thin-film obtained after 12 h. Standard database of PZT (blue bar) and that of the STO (green bar) are also shown for comparison.

performed on the nanostructured films deposited at different hydrothermal reaction periods. **Figure 4**a shows the cross-sectional TEM image of the PZT nano-stub structures formed from the PZT tooth-like seeds after 2 h of hydrothermal treatment. The image indicates the initiation of the hierarchical growth from the PZT seeds as small branches of almost uniform dimension of around 10–15 nm protruding from the top surface of the PZT seed. These protruding branches started to furcate at their tips into smaller branches of size around 5 nm in the product synthesized after 6 h of hydrothermal treatment as shown in Figure 4b. The SAED patterns collected from different zones of these protruding branches indicated the single crystalline nature of the structure (inset to Figure 4b). On further growth after 8 h and 10 h, each of these branches outgrew in size and continued to develop into higher orders of hierarchy (Figure 4c,d) giving rise to a HNh ensemble (Figure 4e) with highest order hierarchical structures of <5 nm in size. HRTEM images from these Nhs near their higher hierarchical branches (area marked in Figure 4d) indicate homo-epitaxial growth following (*l*00) epitaxy as shown in Figure 4f. Closer to the base and near their initiation from the PZT seed (area marked in Figure 4c), hierarchical branches

© 2014 WILEY-VCH Verlag GmbH & Co. KGaA, Weinheim

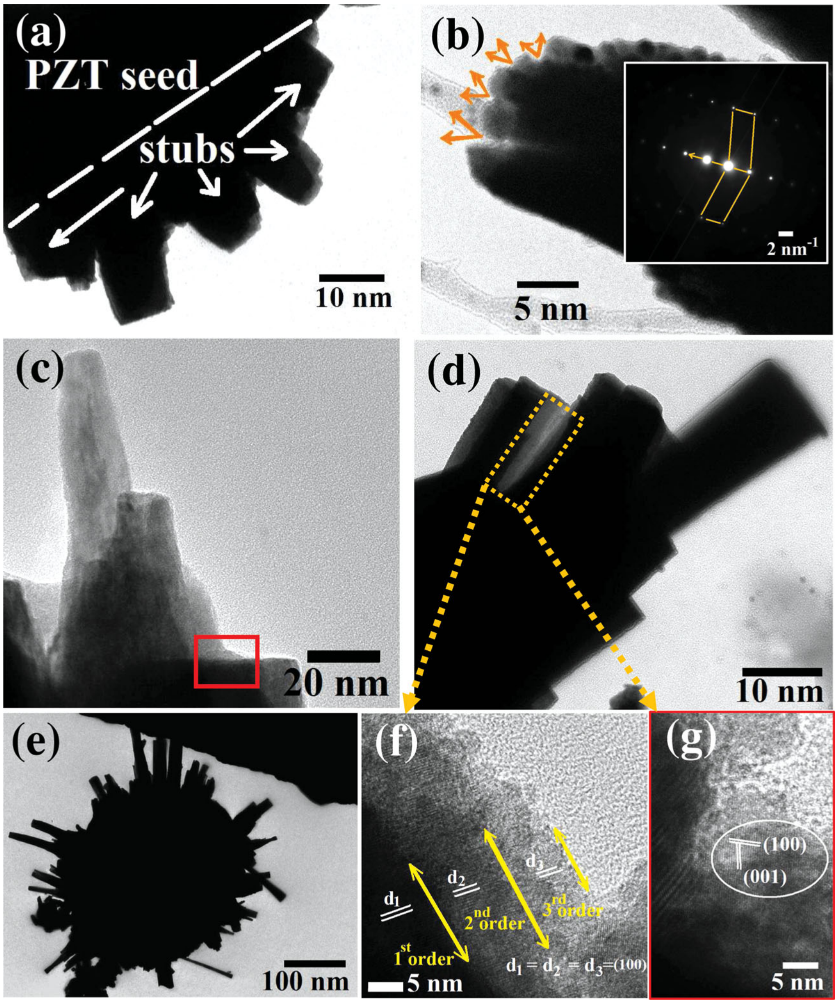

Figure 4. Systematic TEM images of PZT Nhs obtained at different time periods after the hydrothermal treatment of PZT nano-seed layers. a) Growth of PZT nano-stubs from the top surface of the seed after 2 h. b) Closer look at the nano-stub tip indicates multi-furcation with each branch about 5 nm at their base obtained after 6 h. A single crystal SAED pattern shown in the inset reveals similar crystal orientation for the nano-stubs and their branches. (c,d) show multi-level hierarchical growth of PZT nano-branches after 8 h and 10 h. Also showing a fully grown 3D Nh unit after 10 h in (e). f) High resolution TEM image obtained from the marked region in (d) shows the common interfaces of the different order of hierarchical branches and reveals the homoepitaxial nature of the growth mechanism during the final stage of the hierarchy. Here all the hierarchical branches are (100) oriented. g) Heteroepitaxial nature of the crystal planes were (001//100) observed in the initial stage of the HNh (shown by a rectangle in (c)) growth process. Hence a complex hetero-homo epitaxial growth process was presumed to be present.

show hetero-epitaxial growth with planes (*l*00) and (00*l*) occuring at the base of the furcating PZT branches near the top of PZT seeds (Figure 4g). Continuous lattice fringes indicated absence of structural defects in the Nh ensemble.

The microscopic structure of the PZT hierarchical Nh network obtained on the STO:Nb substrate after 12 h of hydrothermal reaction (Figure 3c–e) was studied by cross-sectional TEM (**Figure 5**a). As the image shows, branches of PZT HNhs spontaneously cross-link over a large surface area making them virtually non-penetrable to the electron beam. The interconnecting hierarchical branches (Figure 5b) of adjacent Nhs therefore greatly decrease the porosity of the nanostructured film. Furthermore due to the cross-linked nature of the PZT HNh units, the final nanostructured film obtained after 12 h of hydrothermal reaction treatment is dense with larger surface area and abundant exposed hierarchical branches (see schematic diagram in Figure 5c).

2.4. Growth Mechanism of PZT HNhs

The progressive growth of PZT HNhs from the bottom to the top region indicates that the PZT precursor vapors react from the bottom to the top, which is typically observed in seed-assisted growth of nanostructures.[18,21] High-temperature crystallization during the PLD process promoted the formation of epitaxial nano-seeds of nearly regular shapes (height of almost equal to 50 nm with bottom size of less than 5 nm and top size of about 50 nm). However, as a result of these anisometric dimensions of the PZT seeds (Figure 1a,b), they may possess anisotropic surface energy and the presence of misfit dislocations in the PZT seeds (Figure 1c). Initially a heteroepitaxial growth may have triggered in the PZT Nhs, followed by a more kinetically-controlled homoepitaxial growth of PZT hierarchical branches under a high precursor concentration during hydrothermal reaction.[19,21,32,35] Hierarchical growth in perovskite oxides such as in $PbTiO_3$,[19,32] and $KNbO_3$[32,35–38] nanostructures are also often observed to be controlled by the defects or dislocations present in the crystals. The growth mechanism of the PZT hierarchical Nhs from PZT seeds is schematically shown in **Figure 6**.

2.5. Raman Spectroscopy of PZT Seed-Layer and HNhs

Figure 7 shows the characteristic Raman spectra of the PZT seed-layer film and the nanostructured thin films at different stages of the hydrothermal growth. Typically at room temperature, the FE tetragonal PZT phase with its spontaneous polarization increases the splitting between the E(TO) and A_1(LO) modes,[39–42] which was also observed from the PZT seed-layer and nanostructured thin films. Since Raman modes of nanostructured thin films may characteristically appear to be broad it is difficult to precisely obtain band maxima wavenumber values. In order to be able to unambiguously indentify the wavenumber values of PZT, the spectra were fitted with harmonic Gaussian functions. Six peaks between 100 cm^{-1} and 750 cm^{-1} were identified from the PZT seed-layer (Figure 7a) corresponding to A_1(1TO), E(2TO),

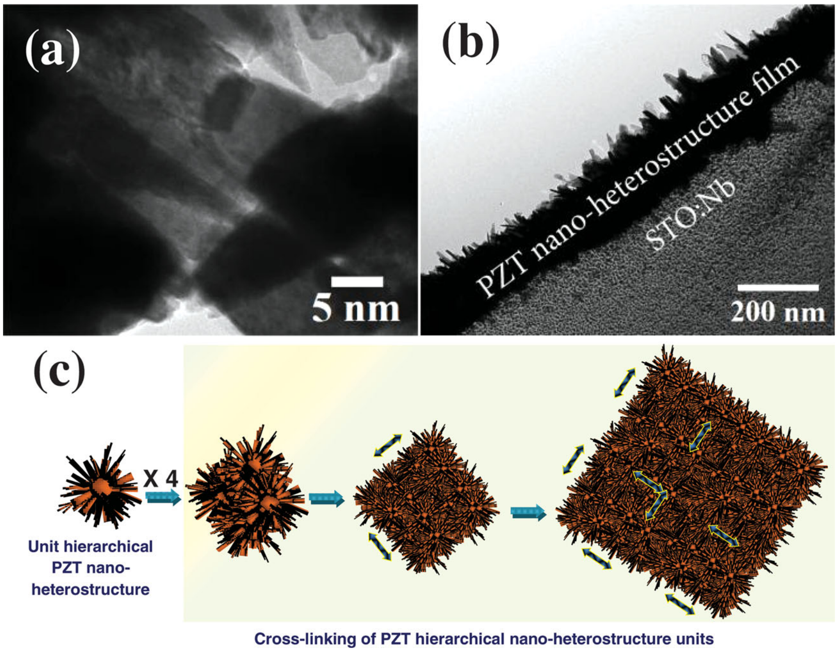

Figure 5. Cross-sectional TEM images of the hierarchical PZT Nh thin-film prepared by milling a 100 nm thick 5 μm x 10 μm rectangular strip from the film surface using a FIB and Pt welding it to a Cu TEM grid. a) Image shows the interlocking phenomenon noticed in closely spaced PZT Nh branches. b) Image showing the dense disposition of the PZT Nh network on STO:Nb substrate. Compact and highly non-porous thin-film allows to measure FE polarization properties without using polymer fill-layer. c) Step-by-step growth of hierarchical PZT Nh network on the substrate by cross-linking and oriented-attachment process.

E(3TO+2LO) i.e., E(silent) + B_1, E(4TO), A_1(3TO), and A_1(3LO) Raman modes, which match with the typical Raman peaks of tetragonal PZT.[39–42] In cases of PZT Nh thin films (at both initial and final stages of growth at 2 h and 12 h, respectively), two additional identifiable frequency peaks (E(1TO) and E(3LO)/A_1(2LO)) and a weakly developed shoulder at about 570 cm^{-1} were observed (Figure 7b,c). Moreover, the Raman spectra shape appear to be anomalous and broadened beyond 700 cm^{-1} in the all nanostructured thin films. While broadness in the Raman spectrum above 700 cm^{-1} was related to the oblique modes between E(3LO) and A_1(3LO),[39–41] the irregular line shape at higher frequencies was correlated with the anharmonic nature of the lattice by Foster et al.[40] The origin of A_1(1TO) peak at about 150 cm^{-1} in tetragonal PZT has also remained a matter of debate. Burns and Scott assigned the 150 cm^{-1} mode as a second-order Raman line, but later the same line was attributed to A_1(1TO) vibration based on polarization considerations and angular dependence of the phonon frequencies.[40,43] The broad 570 cm^{-1} shoulder observed in Nh thin films was related to the continuous distribution of oblique modes between E(3TO) and A_1(3TO). Conclusively, though the Raman peak distribution remains almost analogous, distinct differences in the relative peak intensities were observed as the PZT Nhs were grown from the PZT seeds (Figure 7a–c), which is due to the improvement of crystallinity and increasing development of hierarchy in the PZT Nhs. The observed features also indicate that the PZT seed-layer and Nh films are of virtually single phase with negligibly small strain.

2.6. Ferroelectric Property of PZT HNh Film

Several innovative techniques have been used in recent times to measure the FE properties of PZT nanostructures.[15] The most prevalent technique has been the use of a piezo-force-microscope (PFM) to pole PZT nanostructures and measure their piezoresponse as a function of applied voltage.[44,45] However, since the PFM measures the piezocurrent it cannot provide direct polarization values as typically recorded for PZT thin films. Bharadwaja et al. used a charge-based technique to assess the dielectric and ferroelectric properties of individual mechanically-unconstrained PZT microtubes with interdigitated electrodes.[46] In this regard, another technique that has gained popularity is the embedding of PZT nanostructures in some polymer matrix-host to fabricate their thin-film-type metal/embedded-PZT/metal capacitors for polarization measurements.[14,16] While on one hand the insulating polymer matrix prevents the shorting of the device by filling the pores in the structure, on the other, it introduces huge dielectric losses during the polarization measurements which significantly lowers the polarization values.[16] In our case, however, the significantly reduced porosity and the increased conformity of the dense PZT HNhs formed on the substrate allowed the successful deposition of the Pt-top electrodes without shorting the structures. This enabled the fabrication of Pt/PZT-HNh/STO:Nb thin-film capacitor (where the conducting STO:Nb substrate served as the bottom electrode) as shown schematically in **Figure** 8a, and allowed the successful polarization measurements of the nanostructured PZT films without the need of any polymeric host. The polarization measurements recorded from approximately 20 different Pt-top electrodes while keeping the same bottom electrode showed that almost 80% of the electrodes on the film surface were "not-short" and contributed to consistent *P–E* curves. Further the *P–E* curves measured at different locations on the film surface were found to be consistent with each other (see Supporting Information Figure S2) confirming to the uniform and homogeneous distribution of the PZT Nhs over the entire substrate (Figure 3e and Supporting Information Figure S1).

In Figure 8b, typical room temperature polarization versus electric field (*P–E*) curves have been shown for the Nh PZT thin-film obtained after 12 h of hydrothermal treatment, measured by varying driving voltages from 1 V to 9 V. In order to calculate the electric field (E) (kV cm^{-1}), an average film thickness of 200 nm was used as obtained from the cross-sectional TEM imaging (Figure 5b) of the sample. From the figure it is clearly observed that for driving voltages of 1 V to 3 V the *P–E* curves do not show FE hysteresis or saturation polarization (P_{sat}) indicating a typical dielectric-type behavior. At driving voltage of 4 V the curve registers a remnant polarization (P_r) although it

© 2014 WILEY-VCH Verlag GmbH & Co. KGaA, Weinheim

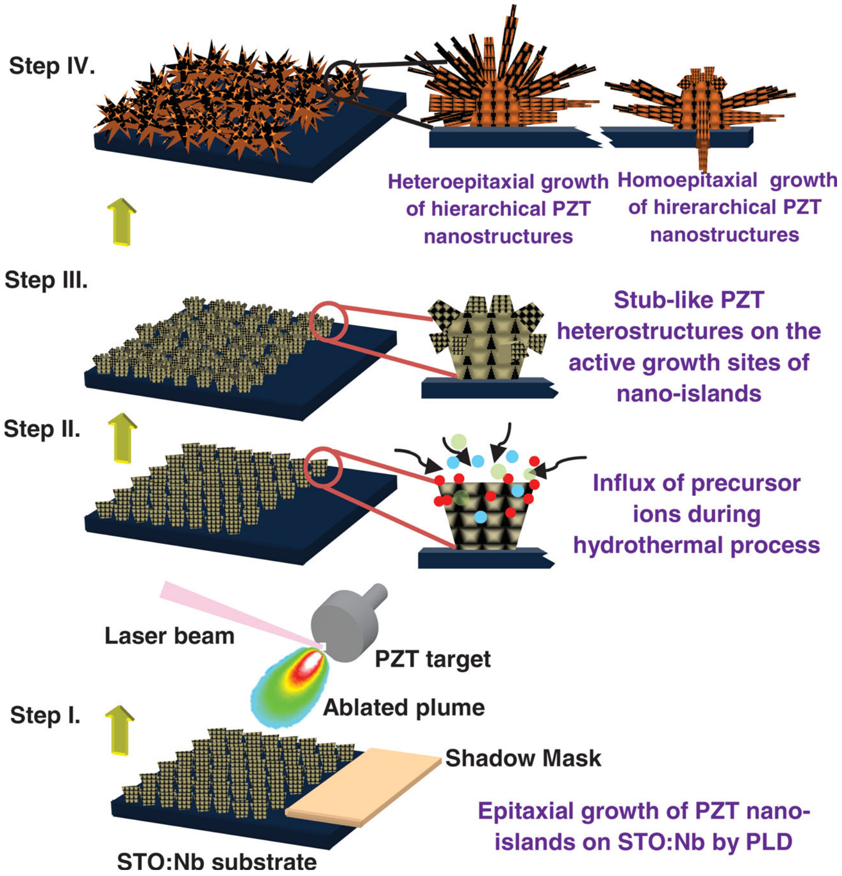

Figure 6. Scheme showing step-by-step growth of hierarchical PZT Nh thin-film starting from the seed-layer growth by PLD process.

is not well-saturated at negative and positive voltages. Similar *P–E* curves with increasing P_r values were also observed for driving voltages of 5 V and 6 V (not shown here). However, for driving voltages of 7 V, 8 V, and 9 V, the *P–E* curves show well-saturated square hysteresis loops with slightly increasing P_r and coercive field (E_c) values with the driving voltages, confirming the FE nature of the sample. The leakage current densities (J_L) measured at varying driving voltages from 1 to 9 V for a stress period of 1 s were consistent with the polarization data. At low voltages of 2 V ($J_L = 6.04 \times 10^{-6}$ A cm^{-2}) and 4 V ($J_L = 1.06 \times 10^{-6}$ A cm^{-2}) when the P-E loops were not saturated, the J_L values were higher than those observed at higher voltages of 6 V ($J_L = 9.59 \times 10^{-7}$ A cm^{-2}), 8 V ($J_L = 9.42 \times 10^{-7}$ A cm^{-2}), and 9 V ($J_L = 9.18 \times 10^{-7}$ A cm^{-2}) when the *P–E* loops showed well-saturated behavior (Supporting Information Figure S3). However, due to the nanostructuring in the PZT-HNh sample, the J_L values were higher than those observed for epitaxial PZT thin films grown by PLD where typical J_L values were 0.43–0.98×10^{-9} A cm^{-2} at 9 V driving voltage.[13] The highest P_r value of 54 µC cm^{-2} at E_c of 237 kV cm^{-1} was recorded at the maximum applied driving voltage of 9 V (Figure 8b). To our knowledge, such high P_r values have been observed for the first time at much lower applied voltages in nanostructured PZT thin films. Earlier Nagarajan et al. had reported a high P_r value of ≈80 µC cm^{-2} at 25 V from island-patterned PZT thin-films.[47] Although the P_r values for such nanostructured PZT thin films cannot be directly compared with those of bulk or thin films because of the differences in surface morphology and grain-size induced effects,[48,49] to our surprise, the recorded P_r values are much higher than chemically grown PZT thin films,[50] and actually as high as those reported for epitaxial PZT thin films grown using PLD.[12,13] Typically, reported P_r values for polycrystalline and oriented tetragonal PZT thin films grown using various techniques such as chemical solution deposition, PLD and sputter deposition vary from 15 to 36 µC cm^{-2}.[6] Our approach to the growth of PZT-HNh thin films produced much higher P_r values as compared to existing reports on PZT nanostructures. Previously Kim et al. had reported a measured P_r value of 1.5 µC cm^{-2} at E_c of 86 kV cm^{-1} for PZT nanotubes embedded in a polymeric host during P-E measurements.[16] On the other hand, the E_c value of 237 kV cm^{-1} recorded at the driving voltage of 9 V for PZT-HNh is much higher than those reported for traditional PZT thin films. Reported E_c values for tetragonal PZT thin films vary from 32 kV cm^{-1} for polycrystalline to 50 kV/cm for epitaxial PZT thin films,[6] with one of the highest E_c values of 86 kV/cm obtained for PZT nanostructures.[16] The high E_c value recorded for PZT-HNh could be attributed to the development of a space-charge layer at the interface of the Pt-top electrode and the PZT nanostructures.[51,52] The surface of PZT Nhs accumulate space-charges which probably got entrapped with the top metal layer deposition creating the space-charge layer. The use of the all-oxide bottom STO:Nb electrode in this case, however, minimized the formation of the space-charge layer at the bottom electrode and PZT interface.[51,53] High squareness (i.e., $P_r/P_{sat\%}$) values of 82 to 85% were recorded for the PZT-HNh thin-film at driving voltages of 7 V to 9 V (see Figure 8). Such high squareness values indicate the nearly-perfect stoichiometric growth of nanostructured PZT-HNh thin-film with tetragonal composition.[54] Also, the P-E loops for nanostructured PZT thin films in Figure 8 are highly symmetric (i.e., $+P_r \approx -P_r$ and $+E_c \approx -E_c$) as compared to the typical aysymmetic loops observed in chemical solution deposited PZT thin films.[55] Since it has been shown that asymmetric *P–E* loops give imprint failures in FE devices as a consequence of high built-in fields, the PZT-HNh thin films grown using this facile synthesis route are better suited for device application.

3. Conclusion

To summarize, hierarchical PZT Nh thin films on STO:Nb substrates were fabricated by a novel and facile physical/chemical combined synthetic-strategy for the first time employing PLD

© 2014 WILEY-VCH Verlag GmbH & Co. KGaA, Weinheim

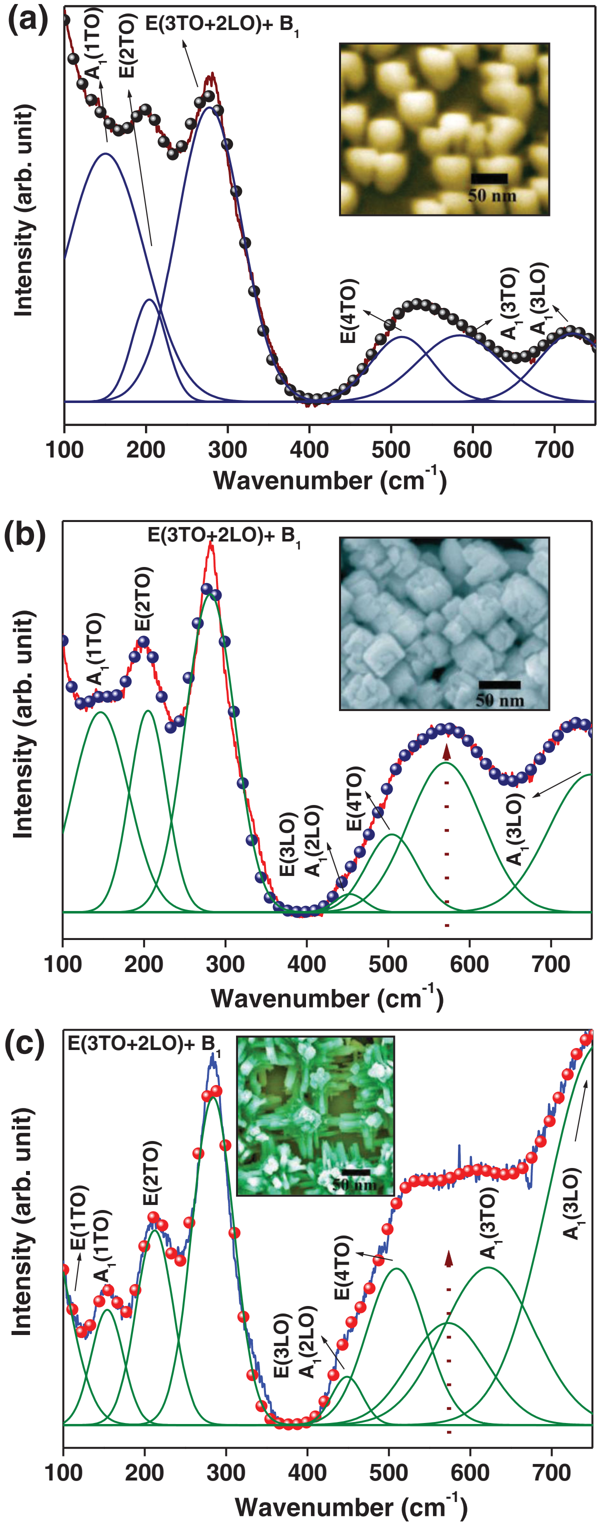

Figure 7. Raman spectra of a) PZT seed-layer thin-film deposited on STO:Nb substrate by PLD, b) PZT nano-stub-like growth after initiation of hierarchy after 2 h of hydrothermal treatment of the seed-layer thin-film, and c) dense PZT Nh thin-film obtained after 12 h of hydrothermal treatment. Rest of the samples showed similar Raman characteristics in agreement to these spectra. Distinct differences in the relative peak intensities were observed with increased development of hierarchy in the PZT Nhs.

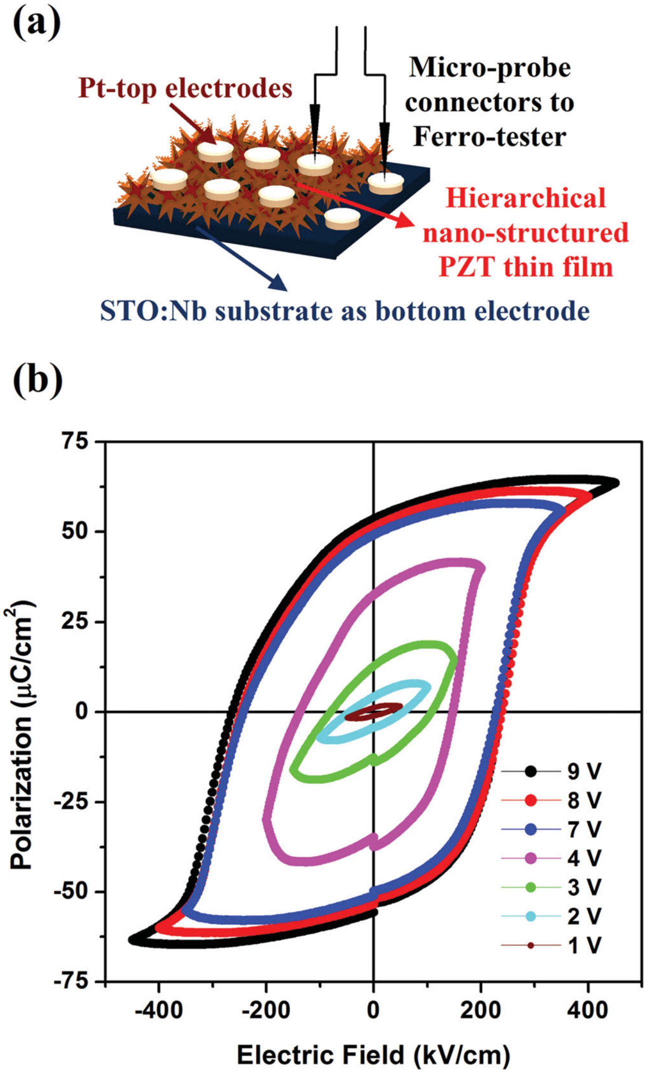

Figure 8. a) Schematic diagram of the PZT nano-structured thin-film capacitor fabricated using Pt-top and the STO:Nb substrate as the bottom electrode for the polarization measurements. b) Polarization versus electric field (*P*–*E*) hysteresis loops for the nanostructured PZT thin-film measured at varying driving voltages from 1 to 9 V.

and hydrothermal processes. The Nhs started to develop heteroepitaxially from PZT seed-layer by controlled nucleation and crystallographically ordered growth, which was carefully monitored by XRD, AFM, SEM, TEM and Raman spectroscopy. As an increased level of hierarchical structure ordering, these 3D nano-hetreostructures cross-link through oriented-attachment and create a dense, nearly non-porous covering over a large surface area on the substrate. Due to this improved nanostructuring density, FE properties could be measured from the Nh PZT capacitor without using polymer fill-layer.[17] As an outstanding improvement, well-saturated FE hysteresis loop with high degree of squareness and P_r value (54 μC cm^{-2} at coercive field of 237 kV cm^{-1}) is realized. This work offers rational synthetic approach towards structurally-ordered PZT and other perovskite materials and opens up new possibilities for the applications of PZT Nhs in various memory storage devices.

© 2014 WILEY-VCH Verlag GmbH & Co. KGaA, Weinheim

4. Experimental Section

Deposition of PZT Seed-Layer by PLD: Initially, a seed-layer of PZT was deposited on highly conducting single-crystal Nb doped $SrTiO_3$ (STO:Nb) (100) substrate using PLD. We used the same growth parameters for the PZT seed-layer as those that led to the growth of high quality epitaxial PZT thin films on STO (100) substrates as in our earlier reports.[12,13] Briefly, a KrF excimer laser (Lambda Physik, wavelength 248 nm, pulse width 30 ns) operating at 10 Hz and providing an energy density of 3 J cm^{-2} at the target surface was used to ablate a non-stoichiometric PZT ($PbZr_{0.52}Ti_{0.48}O_3$ + 30 at% PbO, Kurt J. Lesker) target. The excess PbO in the target was required to overcome the preferential evaporation of Pb during the laser ablation of PZT that lead to Pb-deficient thin films with poor FE properties.[33] A distance of 4 cm was maitained between the target and the substrate during the depositions. Prior to each deposition, the chamber was pumped to a base pressure of 10^{-6} Torr and the target was pre-ablated for 2 min to remove any surface contaminants. During deposition, the substrate was kept at a constant temperature of 550 °C under an ambient oxygen pressure of 500 mTorr. Further a shadow mask was used to preserve an open access to the bottom STO:Nb substrate. After 500 laser pulses (5s), the deposition was stopped and the PLD chamber was flooded with pure oxygen (500 mTorr), while the samples were slowly cooled down to room temperature (approx. 2 h). The thickness of the PZT seed-layer as measured using a profilometer was found to be 400 ± 10 Å.

Synthesis of PZT HNh by Hydrothermal Process:[34] All chemicals (Alfa Aesar) were used as-it-is with a minimum assay of 99.99%. Growth of PZT Nhs were conducted on the pre-deposited and untreated PZT seed-layer on STO:Nb using the hydrothermal process reported earlier. Typically, the reaction solution was prepared by mixing 2 mmol of Ti-n-butoxide ($Ti(OCH_2CH_2CH_2CH_3)_4$) dissolved in 25 mL ethanol, and stoichiometric amount of hydrated zirconium chloride ($ZrOCl_2{\cdot}8H_2O$) dissolved in 25 mL de-ionized water, separately. The Ti ion containing ethanol solution was then added slowly into the Zr ion containing aqueous solution under vigorous stirring. In the next step, 200 mL of NH_4OH solution containing 28–30% of NH_3 was added to this mixture that resulted in a precipitation of intermediate hydroxide phase ($Zr_{0.52}Ti_{0.48}O(OH)_2$). The precipitate was washed and centrifuged several times with water and ethanol in order to remove unreacted chemicals and ionic by-products. After thorough cleaning, the hydroxide precipitate was re-dispersed in 36 mL of de-ionized water. To this solution stoichiometric quantity of hydrated lead nitrate $Pb(NO_3)_2.8H_2O$, 0.02 g PVA (poly(vinyl alcohol)) and 0.4 g PAA (poly(acrylic acid)) were added successively. Required quantity of KOH pellets was added to this mixture to maintain an alkaline pH of ≈ 12. The final growth solution was put into a teflon lined hydrothermal vessel. The substrates were suspended freely midway inside the teflon chamber using a custom designed holder to avoid unwanted material precipitation during the growth process. The chamber with the reactants and the substrate were then sealed and heated at 220 °C for time varying between 4–12 h. After the elapsed time of the reaction, each time the chamber was air cooled and the substrates were cleaned with de-ionized water and ethanol. Uniform, white layers of PZT were obtained every time on the substrates which were air-dried and were used for further characterizations.

Characterizations: The phase purity and crystalline quality of the PZT seed layers and the nanostructured thin films on STO:Nb were characterized by X-ray diffraction (XRD) with a Bruker AXS D8 diffractometer equipped with Lynx Eye position-sensitive detector using Cu Kα radiation ($\lambda = 1.5418$Å). Peak shifts due to sample misalignment was adjusted while performing the XRD scans. Structural analyses of the PZT seed-layer were performed by Digital Instruments' Atomic Force Microscopy (AFM) and scanning electron microscopy (SEM, JEOL JSM 6390 LV). The SEM, transmission electron microscopy and high-resolution transmission electron microscopy (TEM-HRTEM, FEI Tecnai F20 S-Twin TEM) were used to characterize the morphology, size and the intrinsic structure of PZT nanostructured thin films. Energy-dispersive X-ray spectroscopy equipped with the SEM (EDS, Oxford Instruments INCAX sight) was used for the composition analysis of the seed-layer and the nanostructured thin films. The interfacial microstructure in the nanostructured thin films was analyzed by cross-sectional TEM for which the sample was prepared by milling a 100 nm thick 5 μm × 10 μm rectangular strip from the film surface using a focused ion beam (FIB) (JOEL 4500 FIB/SEM) and Pt welding it to a Cu TEM grid. In order to study the structure of the PZT Nhs individually, the material was carefully scrapped out and then dispersed in isopropyl alcohol. Few drops of this solution were then deposited on a carbon coated copper grid and air dried. Raman spectra were measured from the PZT seed-layer and the nanostructured thin films using a Horiba Jobin Yvon T64000 Advanced Research Raman System with a Synapse charge-coupled device (CCD) detection system, and a confocal LabRAM Raman microprobe. The 514.532 nm line of an Ar^+ laser was used for the measurements, which were performed at two different installations. The micro-Raman utility was used by measuring room-temperature spectra under a microscope.

Ferroelectric Polarization Measurement: During the PZT seed-layer growth using PLD a shadow mask was used to cover a part of the bottom STO:Nb substrate and later during the chemical synthesis of PZT nanostructured thin films the masked region was wrapped with Teflon tape so as to preserve an open access to the bottom STO:Nb substrate which served as the bottom electrode during the polarization measurements (Figure 8a). Top Pt electrodes were deposited on the PZT nanostructured thin films using a CRC-100 sputtering system (Plasma Sciences Inc.) and through a shadow mask that produced 100 μm diameter dots for a thickness of 100 nm. The polarization measurements of the fabricated nanostructured PZT thin-film (using Pt-top and Nb doped STO-bottom electrodes) capacitors were performed at room temperature using a commercial Precision LC Ferroelectric tester (from Radiant Technologies, Inc) equipped with a micro-probe station. The polarization data were collected independently from several (more than 20) top electrodes keeping the same bottom electrode and were found to be consistent. During the hysteresis measurements, a constant standard bipolar input profile was used at 100 ms period but varying the driving voltages from 1 V to 9 V. The leakage current densities (J_L) in the thin-film capacitor was measured by applying a stress voltage of 9 V for a period of 1 s (soak time).

Supporting Information

Supporting Information is available from the Wiley Online Library or from the author.

Acknowledgements

This work was partially supported by the Florida Cluster for Advanced Smart Sensor Technologies (FCASST) and the United States Army (Grant No. W81XWH1020101/3349). A.D. and D.M. contributed equally to this paper.

Received: September 23, 2013
Revised: November 14, 2013
Published online: January 3, 2014

---

[1] J. Valasek, *Phys. Rev.* **1920**, *15*, 537.
[2] J. F. Scott, Ferroelectric Memories. Springer Series in Advanced Microelectronics, Vol. *3*, Springer-Verlag, Berlin, Heidelberg, New York **2000**, 248.
[3] M. Dawber, K. M. Rabe, J. F. Scott, *Rev. Mod. Phys.* **2005**, *77*, 1083.
[4] (Ed: R. Waser) Nanoelectronics and Information Technology: Advanced Electronic Materials and Novel Devices, Wiley-VCH, Berlin **2005**.
[5] J. F. Scott, C. A. P. Araujo, *Science* **1989**, *246*, 1400.
[6] J. Schwarzkopf, R. Foranari, *Prog. Cryst. Growth Character. Mater.* **2006**, *52*, 159.

[7] R. Guo, L. E. Cross, S. E. Park, B. Noheda, D. E. Cox, G. Shirane, *Phys. Rev. Lett.* **2000**, *84*, 5423.
[8] N. Izyumskaya, Y.-I. Alivov, S.-J. Cho, H. Morkoç, H. Lee, Y.-S. Kang, *Critical Rev. Solid State Mater. Sci.* **2007**, *32*, 111.
[9] H. Thomann, *Ferroelectrics* **1972**, *4*, 141.
[10] L. W. Martin, Y.-H. Chu, R. Ramesh, *Mater. Sci. Eng. R* **2010**, *68*, 89.
[11] R. Ramesh, S. Aggarwala, O. Auciello, *Mater. Sci. Eng. R: Rep.* **2001**, *32*, 191.
[12] D. Mukherjee, M. Hordagoda, N. Bingham, H. Srikanth, P. Mukherjee, S. Witanachchi, *J. Appl. Phys.* **2012**, *112*, 064101.
[13] D. Mukherjee, R. Hyde, P. Mukherjee, H. Srikanth, S. Witanachchi, *J. Appl. Phys.* **2012**, *111*, 064102.
[14] I. Vrejoiu, M. Alexe, D. Hesse, U. Gösele, *J. Vac. Sci. Technol. B* **2009**, *27*, 498.
[15] A. Gruverman, A. Kholkin, *Rep. Prog. Phys.* **2006**, *69*, 2443.
[16] J. Kim, S. A. Yang, Y. C. Choi, J. K. Han, K. O. Jeong, Y. J. Yun, D. J. Kim, S. M. Yang, D. Yoon, H. Cheong, K. S. Chang, T. W. Noh, S. D. Bu, *Nano Lett.* **2008**, *8*, 1813.
[17] Y. Qi, J. Kim, T. D. Nguyen, B. Lisko, P. K. Purohit, M. C. McAlpine, *Nano Lett.* **2011**, *11*, 1331.
[18] A. Datta, D. Mukherjee, M. Hordagoda, S. Witanachchi, P. Mukherjee, R. V. Kashid, M. A. More, D. S. Joag, P. G. Chavan, *ACS Appl. Mater. Interfaces* **2013**, *5*, 6261.
[19] P. M. Rørvik, T. Grande, M.-A. Einarsrud, *Cryst. Growth Des.* **2009**, *9*, 1979.
[20] P. M. Rørvik, Å. Almli, A. T. J. V. Helvoort, R. Holmestad, T. Tybell, T. Grande, M.-A. Einarsrud, *Nanotechnology* **2008**, *19*, 225605.
[21] J. Y. Lao, J. Y. Huang, D. Z. Wang, Z. F. Ren, *J. Mater. Chem.* **2004**, *14*, 770.
[22] W.-Q. Wu, B.-X. Lei, H.-S. Rao, Y.-F. Xu, Y.-F. Wang, C.-Y. Su, D.-B. Kuang, *Sci. Rep.* **2013**, *3*, 1352.
[23] H. Zheng, Q. Zhan, F. Zavaliche, M. Sherburne, F. Strau, M. P. Cruz, L.-Q. Chen, U. Dahmen, R. Ramesh, *Nano Lett.* **2006**, *6*, 1401.
[24] Z. Wang, Y. Li, R. Viswan, B. Hu, V. G. Harris, J. Li, D. Viehland, *ACS Nano* **2013**, *7*, 3447.
[25] S. M. Baber, Q. Lin, G. Zou, N. Haberkorn, S. A. Baily, H. Wang, Z. Bi, H. Yang, S. Deng, M. E. Hawley, L. Civale, E. Bauer, T. M. McCleskey, A. K. Burrell, Q. Jia, H. Luo, *J. Phys. Chem. C* **2011**, *115*, 25338.
[26] M. A. McLachlan, D. W. McComb, M. P. Ryan, A. N. Morozovska, E. A. Eliseev, E. A. Payzant, S. Jesse, K. Seal, A. P. Baddorf, S. V. Kalinin, *Adv. Funct. Mater.* **2011**, *21*, 941.
[27] X. Y. Zhang, X. Zhao, C. W. Lai, J. Wang, X. G. Tang, J. Y. Dai, *Appl. Phys. Lett.* **2004**, *85*, 4190.
[28] J. Wang, C. S. Sandu, E. Colla, Y. Wang, W. Ma, R. Gysel, H. J. Trodahl, N. Setter, M. Kuball, *Appl. Phys. Lett.* **2007**, *90*, 133107.
[29] X. Chen, S. Xu, N. Yao, Y. Shi, *Nano Lett.* **2010**, *10*, 2133.
[30] T. D. Nguyen, J. M. Nagarah, Y. Qi, S. S. Nonnenmann, A. V. Morozov, S. Li, C. B. Arnold, M. C. McAlpine, *Nano Lett.* **2010**, *10*, 4595.
[31] Y. Qi, J. Kim, T. D. Nguyen, B. Lisko, P. K. Purohit, M. C. McAlpine, *Nano Lett.* **2011**, *11*, 1331.
[32] P. M. Rørvik, T. Grande, M.-A. Einarsrud, *Adv. Mater.* **2011**, *23*, 4007.
[33] D. Mukherjee, R. Hyde, T. Dhakal, H. Srikanth, P. Mukherjee, S. Witanachchi, *Mater. Res. Soc. Symp. Proc.* **2009**, *1199*, 1199-F03–37.
[34] G. Xu, Z. H. Ren, P. Y. Du, W. J. Weng, G. Shen, G. R. Han, *Adv. Mater.* **2005**, *17*, 907.
[35] I. Szafraniak, C. Harnagea, R. Scholz, S. Bhattacharyya, D. Hesse, M. Alexe, *Appl. Phys. Lett.* **2003**, *83*, 2211.
[36] G. K. L. Goh, C. G. Levi, J. H. Choi, F. F. Lange, *J. Cryst. Growth* **2006**, *286*, 457.
[37] M.-R. Joung, H. Xu, J.-S. Kim, I.-T. Seo, S. Nahm, J.-Y. Kang, S.-J. Yoon, *J. Appl. Phys.* **2012**, *111*, 114314.
[38] A. Magrez, E. Vasco, J. W. Seo, C. Dieker, N. Setter, L. Forro, *J. Phys. Chem. B* **2006**, *110*, 58.
[39] G. Burns, B. A. Scott, *Phys. Rev. Lett.* **1970**, *25*, 1191.
[40] C. M. Foster, Z. Li, M. Grimsditch, S. K. Chan, D. J. Lam, *Phys. Rev. B* **1993**, *48*, 10160.
[41] J. Frantti, V. Lantto, J. Lappalainen, *J. Appl. Phys.* **1996**, *79*, 1065.
[42] K. Nishida, M. Osada, S. Wada, S. Okamoto, R. Ueno, H. Funakubo, T. Katoda, *Jap. J. Appl. Phys.* **2005**, *44*, L 827.
[43] M. D. Fontana, H. Idrissi, G. E. Kugel, K. Wojcik, *J. Phys. Condens. Matter.* **1991**, *3*, 8695.
[44] C. S. Ganpule, A. Stanishevsky, Q. Su, S. Aggarwal, J. Melngaillis, E. Williams, R. Ramesh, *Appl. Phys. Lett.* **1999**, *75*, 409.
[45] Y. Luo, I. Szafraniak, N. D. Zakharov, V. Nagarajan, M. Steinhart, R. B. Wehrspohn, J. H. Wendorff, R. Ramesh, M. Alexe, *Appl. Phys. Lett.* **2003**, *83*, 440.
[46] S. S. N. Bharadwaja, P. J. Moses, S. T. McKinstry, T. S. Mayer, P. Bettotti, L. Pavesi, *IEEE Trans. Ultrason. Ferroelectr. Freq. Control.*, **2010**, *57*, 792.
[47] V. Nagarajan, A. Roytburd, A. Stanishevsky, S. Prasertchoung, T. Zhao, L. Chen, J. Melngailis, O. Auciello, R. Ramesh, *Nat. Mater.* **2003**, *2*, 43.
[48] B. A. Hernandez-Sanchez, K.-S. Chang, M. T. Scancella, J. L. Burris, S. Kohli, E. R. Fisher, P. K. Dorhout, *Chem. Mater.* **2005**, *17*, 5909.
[49] C. A. Randall, N. Kim, J.-P. Kucera, W. Cao, T. R. Shrou, *J. Am. Ceram. Soc.* **1998**, *81*, 677.
[50] D. S. L. Pontes, L. Gracia, F. M. Pontes, Beltrán, J. Andrés, E. Longo, *J. Mater. Chem.* **2012**, *22*, 6587.
[51] J. J. Lee, C. L. Thio, S. B. Desu, *J. Appl. Phys.* **1995**, *78*, 5073.
[52] J. F. Scott, *Ferroelectr. Rev.* **1998**, *1*, 1.
[53] J. F. M. Cillessen, M. W. J. Prins, R. M. Wolf, *J. Appl. Phys.* **1997**, *81*, 2777.
[54] J. S. Yang, S. H. Kim, J. H. Yeom, C. Y. Koo, C. S. Hwang, E. Yoon, D. J. Kim, J. W. Ha, *Integr. Ferroelectr.* **2003**, *54*, 515.
[55] a) J. Lee, C. H. Choi, B. H. Park, T. W. Noh, J. K. Lee, *Appl. Phys. Lett.* **1998**, *72*, 3380; b) M. B. Okatan, S. P. Alpay, *Appl. Phys. Lett.* **2009**, *95*, 092902.

© 2014 WILEY-VCH Verlag GmbH & Co. KGaA, Weinheim